ARTICLES

Periodic arrays of gyrotactic plumes in bioconvection

S. Ghorai and N. A. Hill
Department of Applied Mathematics, University of Leeds, Leeds LS2 9JT, United Kingdom

(Received 7 December 1998; accepted 23 September 1999)

Using the continuum model of Pedley *et al.* [J. fluid Mech. **195**, 223 (1988)] for bioconvection in a suspension of swimming, gyrotactic micro-organisms, the existence and stability of periodic arrays of two-dimensional plumes in deep chambers are investigated. The system is governed by the Navier–Stokes equations for an incompressible fluid coupled with a micro-organism conservation equation. These equations are solved numerically using a conservative finite-difference scheme. In sufficiently deep chambers, the plumes are sometimes unstable to varicose or meandering modes. A linear stability analysis for an infinitely deep plume predicts the growth rates of these instabilities and agrees well with the numerical results. © *2000 American Institute of Physics.* [S1070-6631(00)01401-X]

I. INTRODUCTION

Bioconvection is the term used to describe the phenomenon of spontaneous pattern formation in suspensions of micro-organisms such as bacteria and algae (Pedley and Kessler[1]). In all cases, the micro-organisms are 3%–5% denser than water and on average they swim upwards (although the reasons for up-swimming may be different for different species). Micro-organisms respond to certain stimuli by swimming, on average, in particular directions. These responses are called *taxes*, examples being *gravitaxis*, *phototaxis*, *chemotaxis*, and *gyrotaxis*. *Gravitaxis* indicates swimming opposite to gravity, *phototaxis* denotes swimming towards or away from light, and *chemotaxis* corresponds to swimming up chemical gradients. *Gyrotaxis* is swimming directed by the balance of torques due to gravity acting on a bottom-heavy cell and shear flow. We consider gyrotaxis in this paper.

Gravitaxis in small micro-organisms is a passive orientation mechanism unlike active responses to external stimuli such as chemotaxis or phototaxis. In large cells or in multicellular organisms, the force of gravity can be ''sensed'' dynamically by cilia or statically by movable organelles such as statoliths and otoliths. However, such mechanisms are not usually found in the smaller single cells, which are often simply orientated by their own asymmetry. Cells swim randomly but, for example, if a neutrally-buoyant cell is bottom-heavy (i.e. its center of gravity is posterior to its center of buoyancy), the cell will tend to swim vertically upwards in the absence of any other stimuli resulting in (negative) gravitaxis (Kessler[2]). Such cells are also gyrotactic in that a local velocity gradient will produce viscous torques on the cell's body tending to tip it away from the vertical. If the cells do tend to swim upwards, the top layer of the suspension becomes denser than the layer below. When the governing parameters are above critical values, this leads to convective instability and formation of convection patterns. This phenomenon is known as ''bioconvection''; it has some similarity with Rayleigh–Bénard convection, but is driven solely by the swimming of micro-organisms as the following observations make clear. Direct thermal convection can occur in micro-organism suspensions if the containing chamber is heated from below or from the sides, or if sufficient heat is absorbed from the illumination. However, bioconvection continues in a layer that is strongly cooled from below, so it is not a thermal effect (Platt[3]). The radius, a, of a typical gyrotactic cell is approximately 5×10^{-4} cm and the specific gravity is approximately 0.05. The Stokes velocity, which is $2a^2\Delta\rho/9\mu\approx3\times10^{-4}$ cm s^{-1} is 1% of the cells' swimming speed and the patterns disappear when the cells stop swimming.

Plesset and Winet[4] made some measurements of the wavelengths of the bioconvection patterns at the onset of instability in a suspension of the ciliate, *Tetrahymena pyriformis*, which is negatively gravitactic (but not apparently gyrotactic) (Kessler[2]) and showed agreement with the linear stability theory for a layer of dense fluid overlying a layer of light fluid. Kessler[2] demonstrated that many swimming micro-organisms are gyrotactic and made observations (Kessler[5]) of both the almost regular patterns that occur in concentrated algal suspensions in shallow layers a few millimeters deep, and of gyrotactic plume formation in a tall narrow cylindrical tube. Childress *et al.*[6] analyzed the bioconvective instability of a suspension of gravitactic cells, and Pedley *et al.*[7] extended the theory of Childress *et al.*[6] to develop a continuum model for a suspension of *gyrotactic* micro-organisms. Figure 2(d) in the review by Pedley and

 © 2000 American Institute of Physics

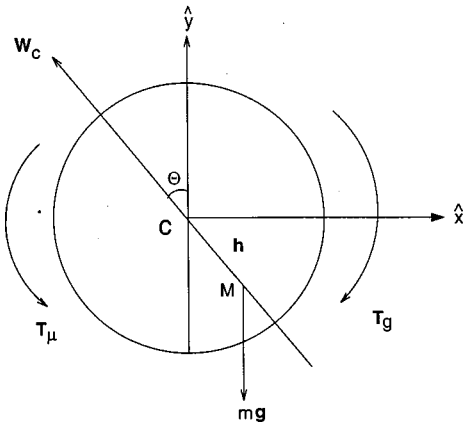

FIG. 1. An idealized algal cell. Θ increases in the anticlockwise sense and $\boldsymbol{h}$ denotes the displacement of the center of gravity from the center of the cell, so that $\boldsymbol{h}=h(\hat{\boldsymbol{x}}\sin\Theta-\hat{\boldsymbol{y}}\cos\Theta)$ relative to Cartesian coordinates, *Cxy*, with the origin at the center of the cell, *C*, and the horizontal, *x*, and the vertical, *y*, directions fixed relative to the laboratory. *M* is the center of mass and $\boldsymbol{W}_c=W_c\,\overline{\boldsymbol{p}}$ is the average swimming velocity of the cell relative to the water. Here $\boldsymbol{p}$ is a unit vector in the swimming direction.

Kessler[1] shows bioconvection plumes in a tall vessel but no quantitative measurements of such plumes in deep chambers have yet been made. The fluid speed generated within bioconvection is typically of the order of 1 mm s^{-1}.

Observations of pattern formation have been recorded previously by such authors as Wager,[8] Loeffer and Mefferd,[9] Wille and Ehret,[10] and Kessler[11] but the results have tended to be of a qualitative nature. A recent quantitative study of bioconvection in algal suspensions was conducted by Bees and Hill,[12] who measured the wavelengths of the planforms of shallow bioconvection patterns as a function of the depth and concentration of the suspension. Hill and Häder[13] measured the trajectories of individual swimming algal cells and showed that their motion is well-characterized by the limit of a correlated, biased, random walk in which the time step tends to zero. They were able to calculate the statistical moments required for the coefficients of the Fokker–Planck equation for the cells' orientational probability density function. These coefficients are needed in Pedley and Kessler's[14] new continuum model.

For simplicity, algal cells such as *Chlamydomonas* (whose shapes closely approximate a spheroid) are idealized here as spheres of radius *a*. Figure 1 shows such a cell placed in a shear flow. Since algal cells are small with typical body diameters of 10–20 μm, and swim at speeds of 100 μm s^{-1}, the Reynolds number associated with swimming is very small and inertia can be neglected. Thus a typical cell swims in a direction $\boldsymbol{p}$ at an angle Θ to the vertical determined by a balance between the gravitational torque, $\boldsymbol{T}_g$, due to its being bottom heavy, and a viscous torque, $\boldsymbol{T}_\mu$, due to fluid-velocity gradients, $\nabla\boldsymbol{u}$, across its body and rotation of the cell, i.e.,

$$\boldsymbol{T}_g+\boldsymbol{T}_\mu=\boldsymbol{0}. \tag{1}$$

This balance is known as gyrotaxis (Kessler[5]). For a sphere of radius *a*, the viscous torque is

$$\boldsymbol{T}_\mu=4\pi\mu a^3(\nabla\times\boldsymbol{u}-2\boldsymbol{\Omega}),$$

where $\boldsymbol{\Omega}$ is the cell's angular velocity and μ is the viscosity of the fluid. The rate-of-strain tensor gives rise to an additional torque on aspherical bodies only (Batchelor[15]). Also, the gravitational torque can be written as

$$\boldsymbol{T}_g=-hm\boldsymbol{p}\times\boldsymbol{g},$$

where *m* is the mass of the cell and $\boldsymbol{g}$ is the acceleration due to gravity. For algal cells, *h* is a few percent of the cell radius. Simplifying Eq. (1), we get

$$\frac{d\Theta}{dt}=\frac{B\zeta-\sin\Theta}{2B}, \tag{2}$$

where ζ is the horizontal component of the vorticity. $B=4\pi\mu a^3/mgh$ is the time scale for the reorientation of the micro-organisms by the gravitational torque against viscous resistance, and it is called the ''gyrotactic orientation parameter'' by Pedley and Kessler.[16]

Thus the gravity and the vorticity can orient individual cells and guide their trajectories. Gyrotaxis can be demonstrated in an experiment in a slow Poiseuille flow down a vertical tube of circular cross section. The balance between gravitational and viscous torques gives one stable equilibrium orientation with individual cells tipped away from the upward vertical towards the axis of the pipe. The cells swim towards the axis as they are carried along in the pipe flow, and focus into a narrow beam. Conversely, if the direction of the flow is reversed, the cells are oriented away from the axis toward the walls, confirming the role of gyrotaxis in cell orientation. Gravity also enters in another, entirely different manner in producing cooperative phenomena (Kessler[5]). The local average fluid density in a suspension is modified by the presence of cells. If there is a small region with a greater than average concentration of cells, the excess density is sufficient to produce a substantial sinking velocity. The sinking region produces a fluid velocity field which guides further gyrotactic accumulation perpendicular to it. This positive feedback generates and maintains the sharply focused descending plumes of cells that are frequently observed in dense algal cultures. The focused beam of algae is often observed to develop an instability in the form of regularly-spaced axisymmetric ''blobs'' (Kessler[5]). The blobs are regions of increased cell concentration, which are wider than the beam. They fall faster than the centerline velocity and therefore have an internal vortex-ring structure. Bioconvection patterns are generated both by purely gravitactic cells and by gyrotactic cells. However purely gravitactic cells accumulate at the top layer and are then swept down plumes by advection, whereas gyrotactic cells converge to the plumes from both the top layer and from the sides of the plume.

Harashima *et al.*[17] solved the equations of bioconvection numerically for purely up-swimming cells (i.e. $\Theta=0$) in a two-dimensional layer of finite depth and width, and studied

the evolution of bioconvection from an initially uniform state. They proposed *minimum potential energy* as a principle for determining the steady-state roll size for a given value of Rayleigh number and a given box size. Their computational domain had a width/height ratio of 8. In contrast, we consider numerical solutions of the equations of bioconvection for *gyrotactic* cells in *deep* chambers using the continuum model of Pedley *et al.*[7] Ghorai and Hill[18] investigated the stability of gyrotactic plumes in a chamber with stress-free side walls. The plumes are stable only in a shallow chamber. As the depth of the chamber is increased, both a varicose and a meandering instability develop and, ultimately, the meandering instability rapidly destabilizes the plume. The growth rate of the meandering mode was higher than that of the varicose mode at moderate wavelengths.

We shall study two-dimensional bioconvection in a layer confined by rigid bottom, stress-free top, and periodic lateral boundaries in the nonlinear regime. The structure and stability of a single plume is examined by varying the gyrotaxis parameter, cell swimming speed, cell concentration, and the depth of the chamber. The plume is steady in a shallow chamber, but becomes unstable as the depth of the chamber is increased. The instability sets in via a varicose mode, where ''blobs'' convect along the plume periodically. Also, a meandering mode sometimes appears, depending on the parameter values. We shall show that the growth rate of the varicose mode is usually higher than that of the meandering mode when the side wall boundary conditions are periodic unlike the case of stress-free side walls (Ghorai and Hill[18]). These two modes and their dependence on the parameters are examined by performing a linear stability analysis for an infinitely long plume. The agreement between the numerical experiments in a finite depth chamber and the linear stability analysis is discussed. We demonstrate that the results of the linear stability analysis do not always agree with the numerical solutions due to the finite depth of the chamber.

II. MATHEMATICAL FORMULATION

The geometry considered consists of a two-dimensional rectangular box of width L and height H referred to Cartesian coordinates with the y-axis pointing upwards. The top wall is stress-free, the bottom wall is rigid and the side walls are periodic. There is no flux of cells through the top and the bottom walls.

A. Governing equations

As in Pedley *et al.*,[7] we assume a monodisperse cell population which can be modelled by a continuous distribution. The suspension is dilute so that the volume fraction of the cells is small and cell–cell interactions are negligible. Each cell has a volume ϑ and density $\rho+\Delta\rho$, where ρ is the density of the water in which the cells swim and $\Delta\rho/\rho \ll 1$. The velocity $\boldsymbol{u}$ is solenoidal and the vorticity, $\boldsymbol{\omega}=\operatorname{curl}\boldsymbol{u}=(0,0,\zeta)$; thus we introduce a stream function ψ such that

$$\boldsymbol{u}=(u,v,0)=\left(\frac{\partial\psi}{\partial y},-\frac{\partial\psi}{\partial x},0\right),\quad \zeta=-\nabla^2\psi. \tag{3}$$

TABLE I. Estimates of typical parameters for a suspension of *C. nivalis*.

Mean concentration	$\overline{n}$	10^6 cells cm^{-3}
Specific gravity	$\Delta\rho/\rho$	0.05
Average radius	a	5×10^{-4} cm
Center of gravity offset	h	10^{-5} cm
Volume per cell	ϑ	5×10^{-10} cm^3
Swimming speed	W_c	10^{-2} cm s^{-1}
Diffusivity of cells	D	5×10^{-4} cm^2 s^{-1}
Kinematic viscosity	ν	10^{-2} cm^2 s^{-1}
Gyrotactic reorientation parameter	B	3.4 s
Typical plume spacing	L	0.5 cm
Scaled swimming speed	$V_c=\dfrac{W_c L}{D}$	10
Schmidt number	$S_c=\dfrac{\nu}{D}$	20
Gyrotaxis number	$G=\dfrac{BD}{L^2}$	10^{-2}
Rayleigh number	$R=\dfrac{\overline{n}\vartheta\Delta\rho g L^3}{\rho\nu D}$	500

Conservation of cells requires that the number of cells per unit volume, n, satisfies the equation

$$\frac{\partial n}{\partial t}=-\nabla\cdot\boldsymbol{J}, \tag{4}$$

where the flux of cells is

$$\boldsymbol{J}=n\boldsymbol{u}+nW_c\overline{\boldsymbol{p}}-D\nabla n. \tag{5}$$

The third term on the right-hand side of Eq. (5) represents the random component of cell locomotion. We assume that the diffusion coefficient D is homogeneous, isotropic and independent of the other parameters of the problem. The second term in Eq. (5) arises due to the swimming of the cells: $W_c\overline{\boldsymbol{p}}$ is the average swimming velocity relative to the fluid and W_c is assumed to be constant. $\overline{\boldsymbol{p}}(\boldsymbol{x},t)$ represents the average orientation of the cells and is estimated from the torque balance equation. The assumptions of constant isotropic D and deterministic $\overline{\boldsymbol{p}}$ in Eq. (5) are ad hoc and modifications have been considered by Pedley and Kessler[14] and Bees *et al.*[19] We retain the simpler form for $\boldsymbol{J}$ in Eq. (5) because it contains the essential features that we wish to model and because improvements lead to quantitative adjustments rather than qualitative changes (Ghorai[20]). Typical values for these parameters are given in Table I based on estimates given by Kessler[21] for a suspension of *Chlamydomonas nivalis*.

The vorticity evolves according to the equation

$$\frac{\partial\zeta}{\partial t}+\nabla\cdot(\zeta\boldsymbol{u})=\nu\nabla^2\zeta-\frac{\Delta\rho g\vartheta}{\rho}\frac{\partial n}{\partial x}. \tag{6}$$

Here ν is the kinematic viscosity and Eq. (6) is derived under the Boussinesq approximation, neglecting all effects of the cells on the fluid except their negative buoyancy, because the suspension is dilute.

B. Calculation of the mean direction

From Fig. 1, we have

$$\boldsymbol{p}\equiv(p_x,p_y)=(-\sin\Theta,\cos\Theta),$$

where Θ is the solution of Eq. (2). If the shear is sufficiently small so that $|B\zeta|\leqslant 1$, then the steady-state orientation is obtained by setting the left hand side of Eq. (2) equal to zero. When $|B\zeta|\leqslant 1$, we find that

$$\overline{\boldsymbol{p}}=(-\kappa,(1-\kappa^2)^{1/2}),\ |\kappa|\leqslant 1, \tag{7}$$

where $\kappa=B\zeta$. If the vorticity is large ($|B\zeta|>1$), the cell tumbles but swims on average in a fixed direction at an angle to the vertical (Kessler[5]). When the vorticity is large, the average swimming direction $\overline{\boldsymbol{p}}$ is approximated by integrating the swimming direction over the tumbling period (Ghorai and Hill[18]).

If $\kappa=B\zeta>1$, then

$$\overline{\boldsymbol{p}}=(-\kappa+(\kappa^2-1)^{1/2},0) \tag{8}$$

and similarly, if $\kappa=B\zeta<-1$, then

$$\overline{\boldsymbol{p}}=(-\kappa-(\kappa^2-1)^{1/2},0). \tag{9}$$

Equations (7), (8), and (9) determine the average swimming direction of the cells for any value of ζ.

The equations are scaled using the width L, the time scale L^2/D, and the mean concentration $\overline{n}$. The resulting system of coupled equations is

$$\boldsymbol{u}=(u,v,0)=\left(\frac{\partial\psi}{\partial y},-\frac{\partial\psi}{\partial x},0\right),\ \zeta=-\nabla^2\psi, \tag{10}$$

$$\frac{\partial\zeta}{\partial t}+\boldsymbol{\nabla}\cdot(\zeta\boldsymbol{u})=S_c\nabla^2\zeta-S_cR\frac{\partial n}{\partial x}, \tag{11}$$

and

$$\frac{\partial n}{\partial t}=-\boldsymbol{\nabla}\cdot\boldsymbol{J}, \tag{12}$$

where the flux of cells is

$$\boldsymbol{J}=n\boldsymbol{u}+nV_c\overline{\boldsymbol{p}}-\boldsymbol{\nabla}n. \tag{13}$$

Here $S_c=\nu/D$ is the Schmidt number, $V_c=W_cL/D$ is the scaled cell swimming speed, and R is a Rayleigh number, defined as

$$R=\frac{\overline{n}\vartheta\Delta\rho gL^3}{\rho\nu D}.$$

The definition of R is nonstandard in that it is based on the width of the chamber and on the mean cell concentration, rather than the height and cell concentration at the top of the layer. The conventional Rayleigh number, R^* say, used by Hill *et al.*[22] is related to our definition by

$$R^*=RV_c\lambda^4/(1-\exp(-V_c\lambda)),$$

for a given aspect ratio $\lambda=H/L$, and it increases with an increase in the height of the chamber, whereas ours remains constant. Our choice for the length and the time scales ensures that the height of the chamber can be varied independently of the other parameters. Note also that the bioconvection equations reduce to those of the thermal convection when $V_c=0$. $\overline{\boldsymbol{p}}$ is defined by Eqs. (7)–(9), where $\kappa=G\zeta$ and $G=BD/L^2$ is the dimensionless gyrotaxis number. The dimensionless gyrotaxis number represents the ratio of the reorientation time due to gyrotaxis to the diffusion time. The boundary conditions are applied at

$$x=\pm\tfrac{1}{2}\text{ and }y=0,\lambda.$$

C. Initial and boundary conditions

We impose rigid, no-slip boundary conditions at the bottom wall, stress-free boundary conditions at the top wall and no flux of cells through them, so that

$$\begin{aligned}&\psi=\frac{\partial\psi}{\partial x}=\boldsymbol{J}\cdot\hat{\boldsymbol{y}}=0\ \text{ at }y=0,\lambda,\\&\frac{\partial\psi}{\partial y}=0\ \text{ at }y=0,\ \frac{\partial^2\psi}{\partial y^2}=0\ \text{ at }y=\lambda.\end{aligned} \tag{14}$$

The vertical side walls are periodic and thus

$$\psi(-\tfrac{1}{2})=\psi(\tfrac{1}{2}),\ \zeta(-\tfrac{1}{2})=\zeta(\tfrac{1}{2})\text{ and }n(-\tfrac{1}{2})=n(\tfrac{1}{2}). \tag{15}$$

The initial conditions are that of a uniform state together with a small perturbation to the uniform concentration of cells,

$$\psi=0,\ \zeta=0,\text{ and }n=1+\epsilon\cos(m\pi x), \tag{16}$$

where $\epsilon=10^{-5}$ and $m=2$. The perturbation is applied for computational convenience to ensure that the plume forms in the middle of the chamber.

III. NUMERICAL PROCEDURE

The governing Eqs. (10)–(12) are discretized using a conservative finite-difference scheme (Ghorai[20]) on a staggered mesh with the stream function and vorticity stored on one set of nodes and the concentration stored on another set of nodes. The grid is chosen so that the concentration nodes lie in the interior only, whereas those of the stream function and vorticity lie in the interior and also on the boundary of the domain. The advantage of the staggered mesh is that the no-cell flux boundary condition can be satisfied immediately

when discretized, without further approximation. We know that a plume is concentrated along a narrow column and that there are boundary layers at the top and bottom walls due to the large cell concentration and the presence of the rigid wall, respectively. In order to resolve these gradients accurately, a nonuniform coordinate mesh is used. We transform the nonuniform spatial increments Δx_i and Δy_j in the finite difference equations to a uniform grid using an orthogonal transformation $\xi_k = \xi_k(x_k)$ which also maps the problem to the computational domain $-1 \leqslant \xi_k \leqslant 1$, where $x_k = (x,y)$ and $\xi_k = (\xi, \eta)$. An accurate transformed finite difference equation for the first order derivative is given by

$$\frac{f_{i+1} - f_{i-1}}{2\Delta\xi (dx/d\xi)_i} = f_i^I \left[1 + \frac{(\Delta\xi)^2}{6} \left(\frac{d^3x}{d\xi^3} \right)_i \Big/ \left(\frac{dx}{d\xi} \right)_i \right] \quad (17)$$

(de Rivas[23]). Here f_i is the value of the function $f(x)$ at the ith node and f_i^I is the first order derivative at the ith node. The second term inside the bracket on the right-hand side of Eq. (17) is important only when there is a large grid variation. The second-order difference operator is obtained by recursion of Eq. (17). The above difference approximation has a truncation error of $O(\Delta\xi^2)$ for an arbitrary mesh transformation in problems of boundary layer character. Here we have taken the transformations proposed by Roberts.[24]

An expression for the vorticity boundary condition can be obtained by expanding the stream function near the rigid surface using a three-term Taylor series expansion and by making use of no-slip condition,

$$\zeta_w = -\frac{\zeta_{nw}}{2} - 3.0 \frac{\psi_{nw}}{(\Delta n)^2}, \quad (18)$$

where ζ_{nw}, ψ_{nw} are the values of ψ, ζ at the near-wall node (adjacent to the wall) and Δn is the nondimensional distance of the near-wall node from the wall.

An implicit scheme with Euler backward differencing in time and central differencing in space is used to obtain the transient solutions. A line-by-line cyclic tridiagonal matrix algorithm with relaxation is used to solve the nonlinear discretized equations. The number of grid points along the x direction is 36 and the number of grid points along the y direction is increased with an increase in aspect ratio. For example 36 points are taken for $\lambda = 1$ and 56 points are taken for $\lambda = 4$ along the vertical direction. Some of the results were run with different numbers of grid points to check the grid independence of the solutions. If the swimming speed is zero then the equations of bioconvection are similar to those of the heat convection problem. To validate the code, written in terms of stretched coordinates, the code has been run for the heat convection problem and the agreement with the benchmark solution of de Vahl Davies[25] (Ghorai[20]) is good. The code has also been used to compute the critical Rayleigh numbers against wavelengths (Ghorai and Hill[18]) and the agreement with the linear stability results of Hill *et al.*[22] is excellent.

IV. RESULTS

Equations (10)–(12) possess a static solution with $\psi = \zeta = 0$ and an equilibrium exponential concentration profile,

$$n_p(y) = \frac{V_c \lambda \exp(V_c y)}{\exp(V_c \lambda) - 1}. \quad (19)$$

If the governing parameters are above the critical values, the concentration profile develops from the initially uniform state towards Eq. (19), but bioconvection begins before the profile develops fully. In the following discussions, we consider physically relevant parameter values based on a chamber width (or periodic spacing) of approximately 0.5 cm using data from Table I.

A. Effect of the aspect ratio

To study the effect of the depth on plume formation, the governing parameters R, S_c, G, V_c are kept constant at physically relevant values (see Table I),

$$R = 500,\ S_c = 20,\ G = 0.01 \text{ and } V_c = 10, \quad (20)$$

and the aspect ratio is varied from small to large values.

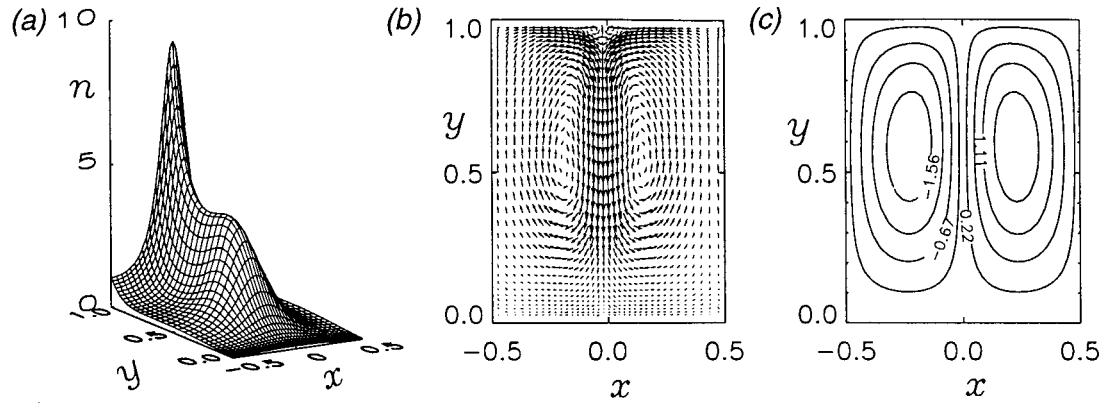

FIG. 2. Steady-state plume for aspect ratio $\lambda = 1$ with periodic side walls; (a) concentration, (b) cell fluxes, (c) streamlines (with equally spaced contour levels).

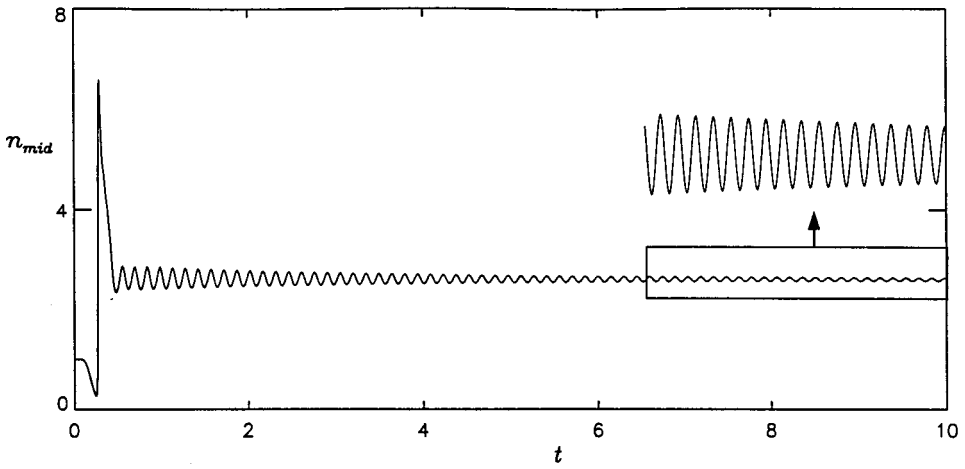

FIG. 3. Variation of $n_{\mathrm{mid}}=n(0,2)$ against time for aspect ratio $\lambda=4$. The decreasing amplitude of the fluctuations suggests that the plume solutions are approaching the steady-state slowly.

For aspect ratio $\lambda=1$, the evolution of the plume is similar to the stress-free side walls case (Ghorai and Hill[18]). Initially the cells accumulate at the top and form a plume in the middle of the two-dimensional box due to the perturbation to the initial uniform concentration of cells. The plume becomes steady after a short period of time. The final steady-state of the plume is shown in Fig. 2. In this figure are plotted (a) the concentration profile as a surface, (b) the total cell flux vector $\boldsymbol{J}$, and (c) the streamlines. The final state of the plume is also steady for $\lambda=2$, but it takes longer to reach the final state and the solutions in the mid-region of the plume are almost independent of the vertical coordinate. A small blob appears at an early stage and starts convecting down the plume periodically but it gradually disappears as the final steady-state is reached. For $\lambda=4$, the variation of the central concentration, $n_{\mathrm{mid}}=n(0,2)$, at the midpoint of the chamber is plotted in Fig. 3. It shows that the amplitude of the fluctuation decreases much more slowly.

The case when $\lambda=5$ is different from the previous cases. We have shown the evolution of the concentration (as contours) from the initial uniform state in Fig. 4. When the head of the plume hits the bottom of the chamber [Fig. 4(d)], a small blob develops just above it. This blob disappears rapidly for small aspect ratios, e.g., $\lambda=1,2$, and much more

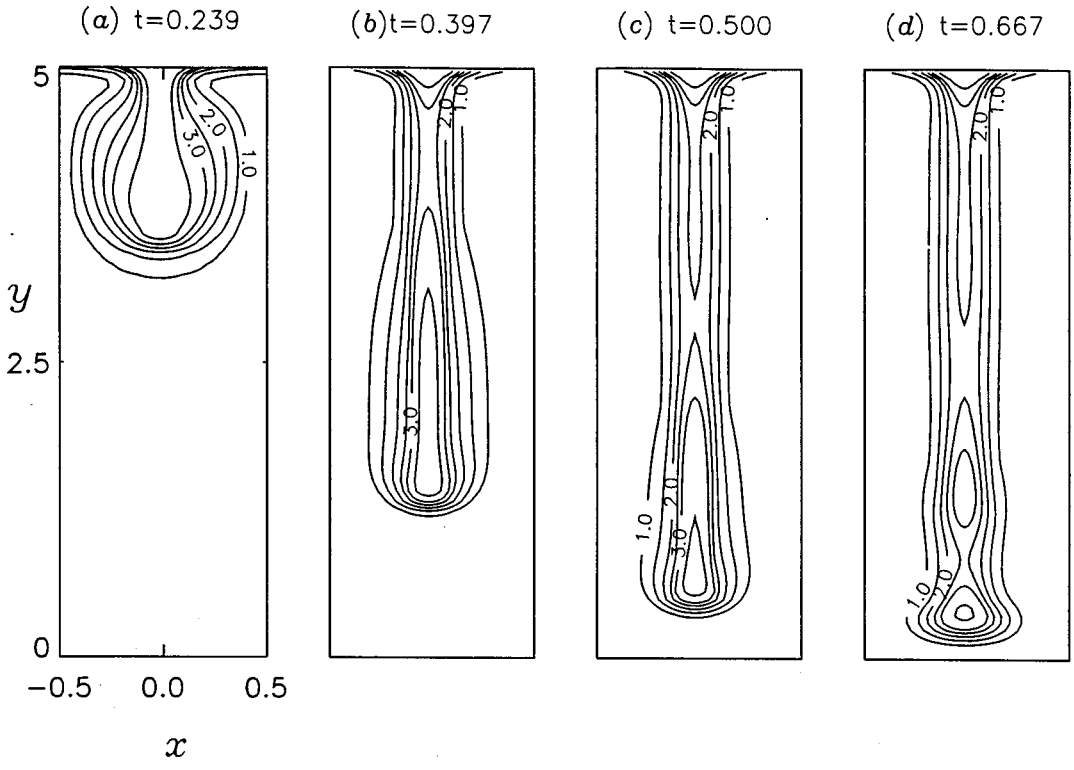

FIG. 4. Evolution of the plume at successive times plotted as concentration contours for aspect ratio $\lambda=5$ with periodic side walls.

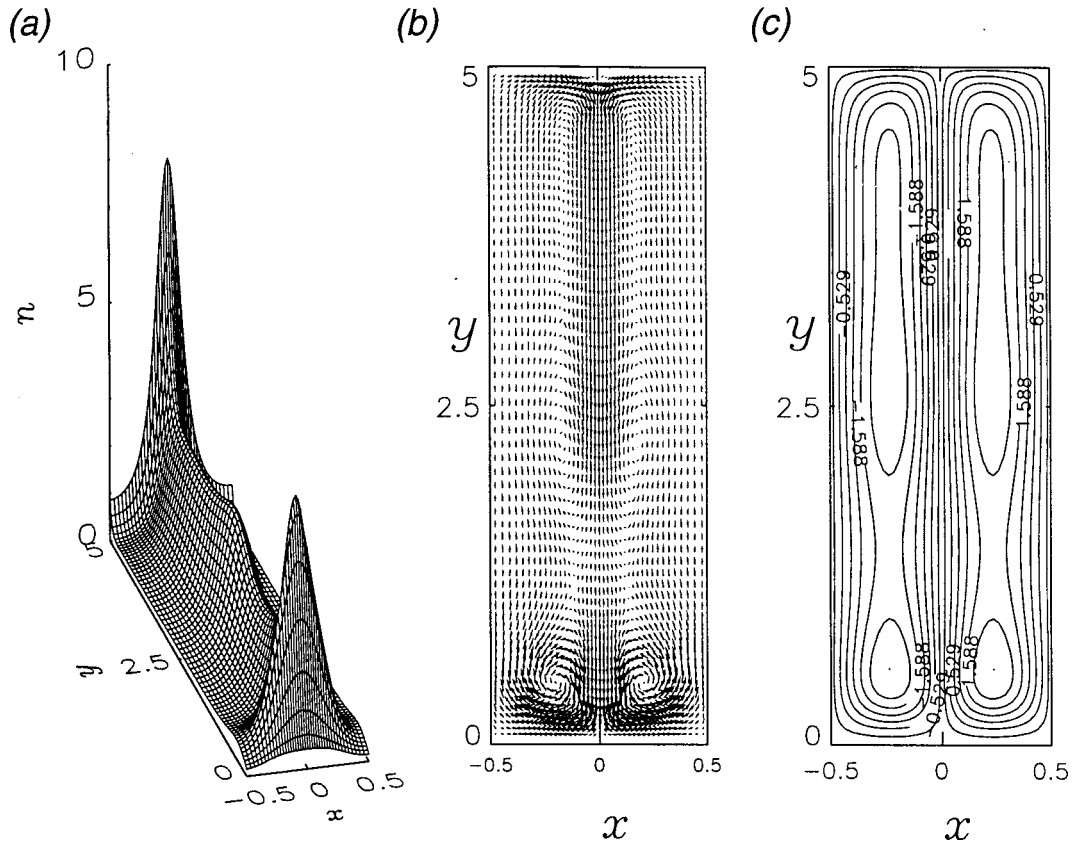

FIG. 5. Snapshot of (a) concentration, (b) cell fluxes, and (c) streamlines for periodic blob convection at an aspect ratio $\lambda = 5$ with periodic side walls.

slowly for aspect ratio $\lambda = 4$, but in this case ($\lambda = 5$), it convects along the plume periodically. Figure 5 shows a snapshot of the periodic blob convection where the blob is approximately at the mid-height of the chamber. Figure 5(b) shows that some of the cells are recirculating at the bottom of the plumes and the rest are advecting upwards. Some of these upwards swimming cells are attracted to the blob due to the circulation and the others swim to the top of the chamber. When this blob hits the bottom of chamber, then it forces a fraction of the cells (circulating at the bottom) to advect upwards and during this time another blob starts to develop near the top of the plume. The variation of the central concentration, $n_{\mathrm{mid}} = n(0, 2.5)$, at the midpoint of chamber against time is plotted in Fig. 6. It shows that this blob convection is periodic with a period of approximately 0.15 units. Figure 7 shows four snapshots of concentrations during one cycle of the oscillation. Figure 7(a) shows the blob about to hit the bottom of the chamber. Figure 7(b) shows it just after hitting the bottom of the chamber with another small blob having developed from the top of the plume. Figure 7(c) shows the new blob as it crosses the mid-height of the chamber and Fig. 7(d) completes the full cycle. Thus the final state of the plume is periodic and the final state undergoes a Hopf bifurcation as the aspect ratio, λ, is increased from 4 to 5.

When the aspect ratio is increased to 8, the number of blobs convecting along the plume at any instant is two, and the concentration contours during one cycle of the oscillation

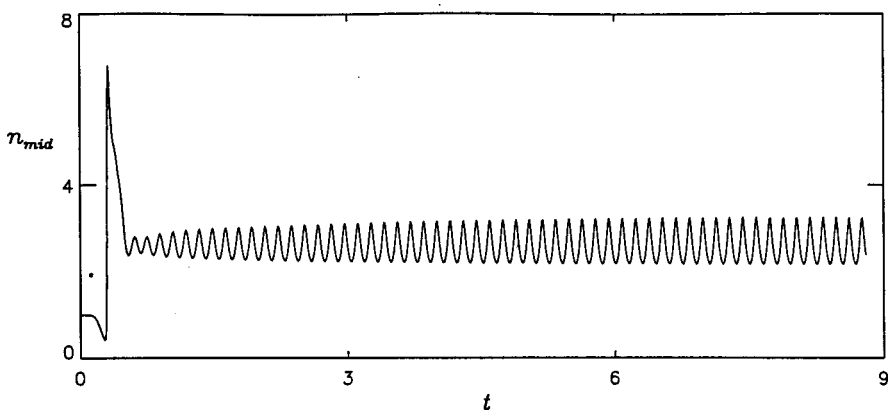

FIG. 6. Variation of $n_{\mathrm{mid}} = n(0,2.5)$ against time for aspect ratio $\lambda = 5$. It shows that the plume becomes periodic after $t = 5$ approximately. The fluctuations correspond to blobs crossing the mid-height of the chamber.

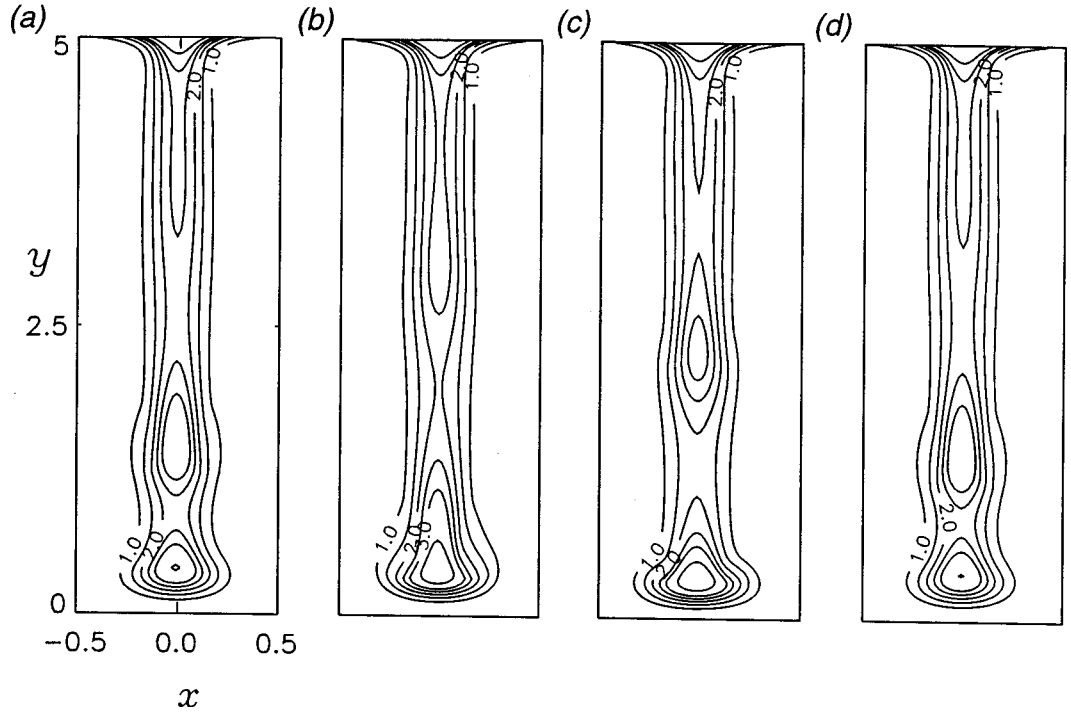

FIG. 7. One cycle of the oscillation in concentration (plotted as equally spaced contour levels) for aspect ratio $\lambda = 5$. The intervals between plots (a)–(d) are equal and the period is approximately 0.15 units.

are shown in Fig. 8. Figure 8(a) shows one blob descending near the middle of the chamber and the other one three-quarters of the way down the chamber. The next figure shows the first blob after it has crossed the mid-height and the second blob has hit the bottom of the chamber. During this time a new blob has formed at the top of the plume. Figure 8(c) shows two blobs descending along the plume and Fig. 8(d) completes the full cycle. Thus, as the aspect ratio of the chamber increases, the number of blobs increases, so the wavelength of the varicose mode is finite. The distance be-

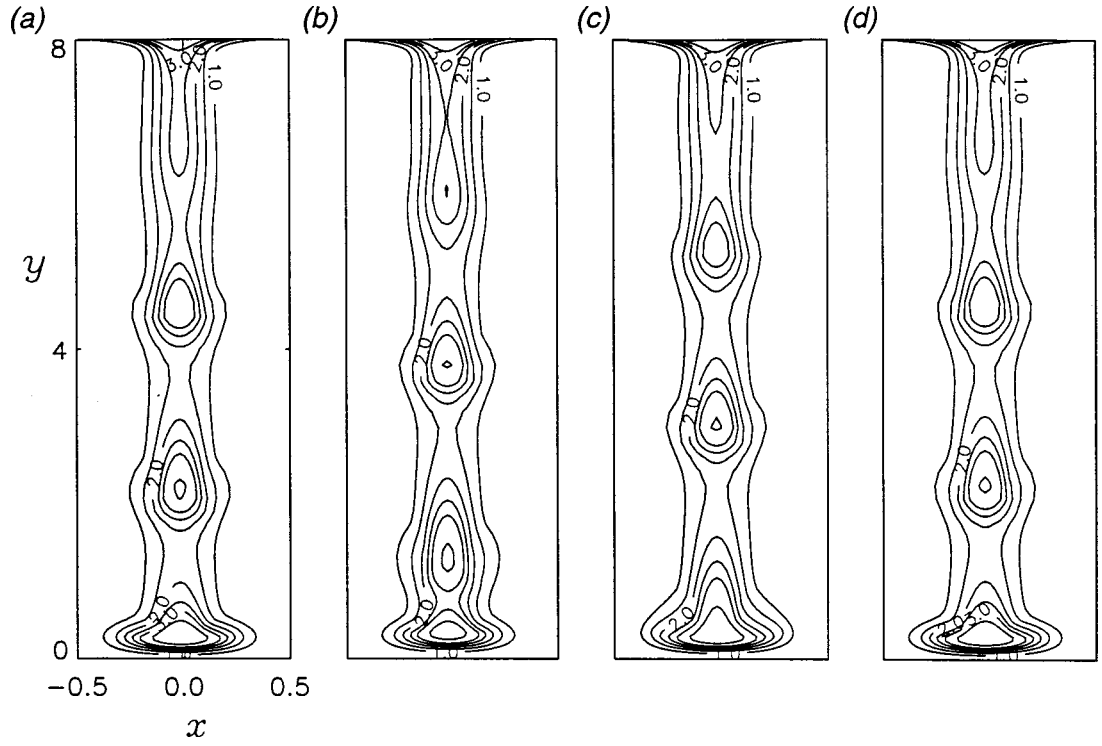

FIG. 8. One cycle of the oscillation in concentration (plotted as equally spaced contour levels) for aspect ratio $\lambda = 8$. The intervals between plots (a)–(d) are equal and the period is approximately 0.15 units.

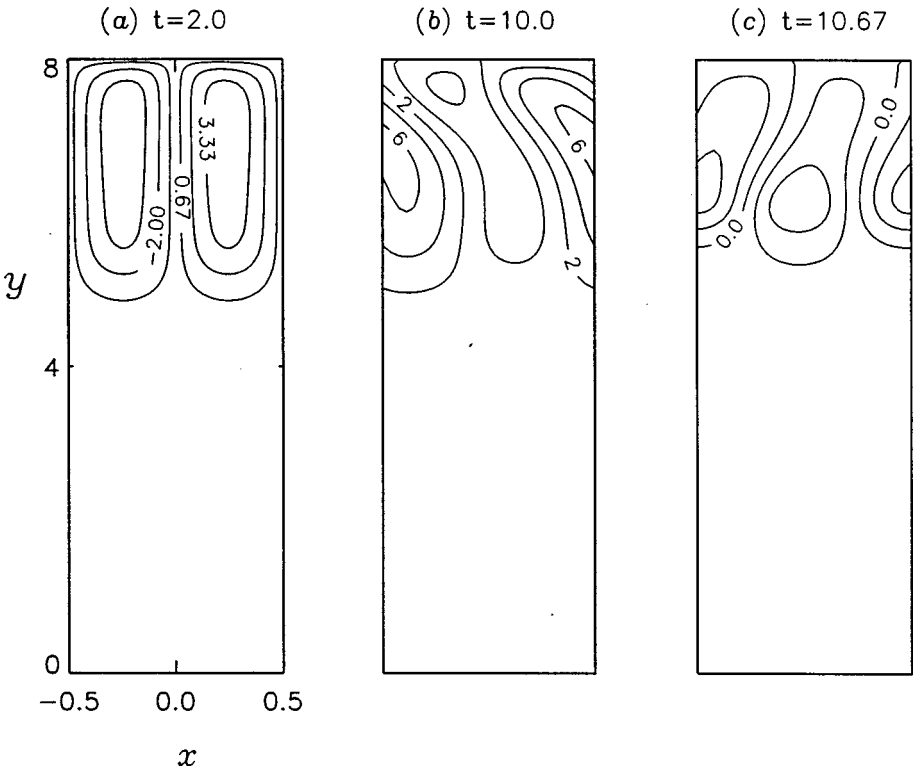

FIG. 9. Dependence of plume on gyrotaxis number in a deep chamber of aspect ratio $\lambda=8$ for $G=2.5\times10^{-3}$; snapshots of streamlines for (a) initial apparently-steady state at $t=2.0$, (b) movement of the plume to the right at $t=10.0$, and (c) movement of the plume to the left at $t=10.7$.

tween the blobs is approximately 2 cm in dimensional units. Only the varicose instability appears for the set of parameter values given by Eq. (20). On the other hand, this varicose mode and a meandering mode appear for the same parameter values in simulations with stress-free side walls (Ghorai and Hill[18]) and the meandering mode dominates the varicose mode for aspect ratio $\lambda>2$.

B. Effects of the gyrotaxis number

In this section we investigate the dependence of the final state of the plume on the gyrotaxis number, G, for a large aspect ratio $\lambda=8$ of the chamber. We fix the following parameter values,

$$R=5\times10^{2},\ S_c=20,\ V_c=10 \text{ and } \lambda=8. \tag{21}$$

The parameter values given by (21) are derived from a cell swimming diffusion coefficient $D=5\times10^{-4}$ cm^2 s^{-1} and a chamber width $L=0.5$ cm (see Table I). The value of $G=BD/L^2$ based on $B=3.4$ s (Pedley and Kessler[1]) is approximately 7×10^{-3}. Thus we vary G from 2.5×10^{-3} to 1.7×10^{-2} to cover a range of physically relevant values. The initial conditions are given by Eq. (16). At an early stage of plume formation, blobs appear in all the cases considered in this section. Ultimately these blobs disappear for a certain range of values of G, but remain in the final state for a different range of values of G. Details of the computations are presented below.

For $G=2.5\times10^{-3}$, the plume extends to less than half of the depth of the chamber. The blobs, which appear at an early stage, soon disappear and the plume appears to be steady as shown in streamlines in Fig. 9(a). However, ultimately, this plume becomes unstable to a meandering mode at around $t=8.5$ and moves towards the right side of the chamber [Fig. 9(b)] and then towards the left side of the chamber [Fig. 9(c)]. The concentration at the point $(x,y)=(0,7)$ near to the top of the central axis of the chamber is plotted against time in Fig. 10. The solution at an early stage ($t<4$) is of periodic blob convection. This blob convection dies down and the plume remains apparently in a steady-state for $4<t<8.5$. The meandering mode destabilizes the plume

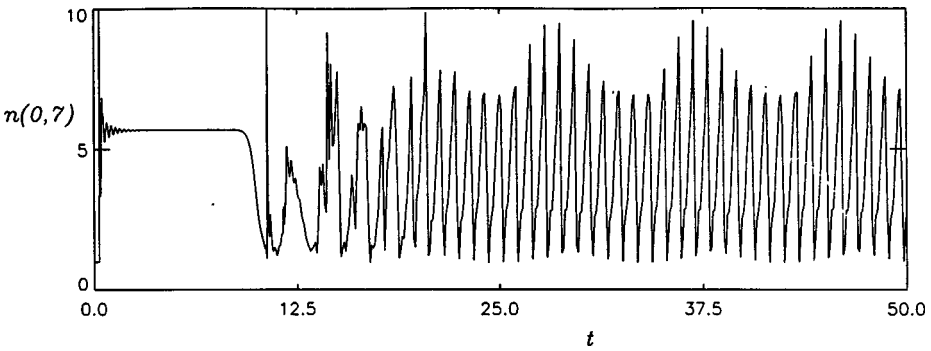

FIG. 10. Variation of the concentration at the point $(x,y)=(0,7)$ with $G=2.5\times10^{-3}$ for aspect ratio $\lambda=8$ for the plume shown in Fig. 9.

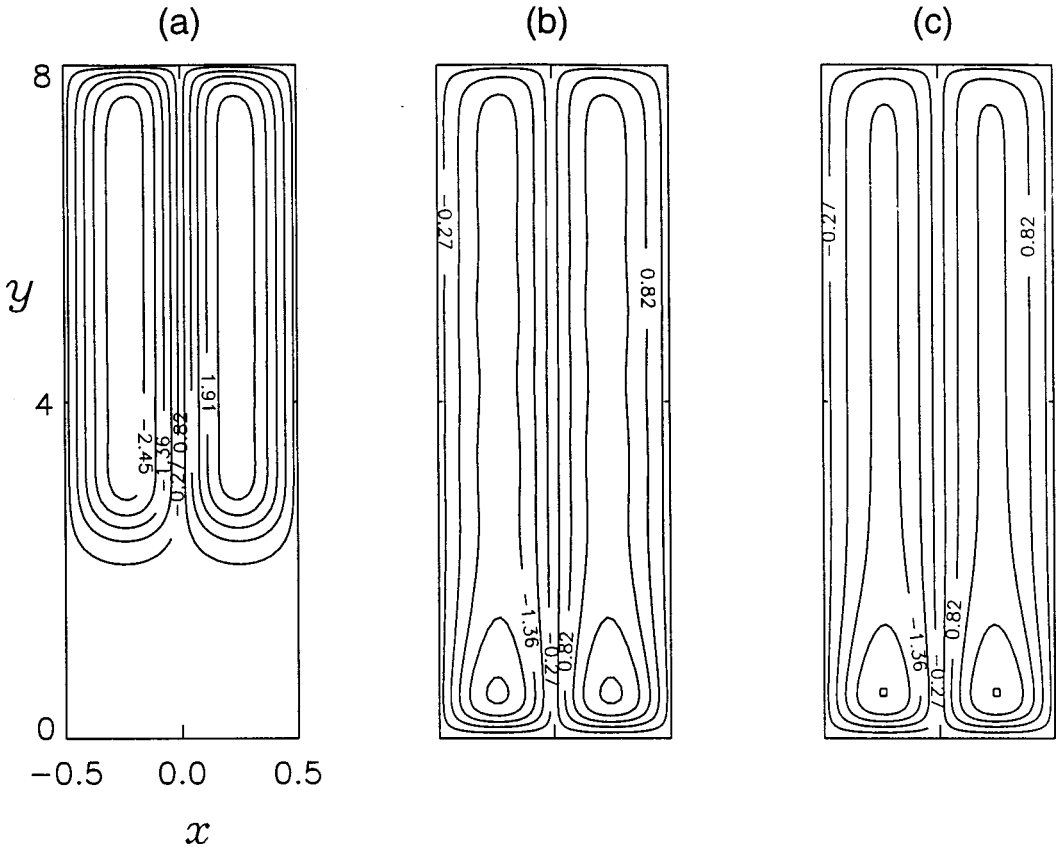

FIG. 11. Dependence of the plume on gyrotaxis number in a deep chamber of aspect ratio $\lambda=8$; snapshots of streamlines for (a) $G=6\times10^{-3}$, (b) $G=0.015$, (c) $G=0.017$. In (a) and (c) the final state is steady but in (b) there is periodic blob convection along the plume. (See also Fig. 8, where $G=0.01$.)

at about $t=9.0$. The final state of the plume appears to be almost doubly periodic, where the plume oscillates from left to right and then from right to left with a periodically modulated amplitude.

For $G=6\times10^{-3}$, the plume extends to almost three-quarters of the depth of the chamber and the final state is steady [Fig. 11(a)]. The solution in the mid-region of the plume is almost independent of the vertical coordinate. This solution becomes periodic with two blobs convecting along the plume when G is increased to 0.01 (see Sec. IV A and Fig. 8). This blob convection persists at $G=0.015$, but the size of the blobs becomes smaller and at $G=0.017$, these blobs disappear [see Figs. 11(b) and 11(c)]. As the value of G increases, the concentration of cells at the bottom of the chamber also increases.

C. Effects of the cell swimming speed

Here the values of R, G, S_c, and λ are kept fixed and V_c is varied from 5.0 to 12.0. The following values are taken for the fixed parameters:

$$S_c=20,\ G=10^{-2},\ R=500,\ \text{and}\ \lambda=8 \tag{22}$$

(see Table I). In all the runs described here, blobs appear at an early stage. For $V_c=5$ and $V_c=8$, the plumes do not extend down to the bottom of the chamber and the final states of the plume are steady [see Fig. 12(a) and 12(b)]. The length of the plume for $V_c=8$ is greater than that of $V_c=5$ and the time to reach the steady state is longer for $V_c=8$ than $V_c=5$. This solution becomes periodic with two blobs convecting along the plume when V_c is increased to 10 (see Sec. IV A and Fig. 8). This varicose convection persists at $V_c=12$ [Fig. 12(c)], but the size of the blobs does not diminish unlike the large G cases, in which the blobs almost disappear at higher values of G. As the value of V_c increases, the concentration of cells at the bottom of the chamber also increases.

D. Effects of the Rayleigh number

We investigate the effect of varying the Rayleigh number on the stability of a single plume in a chamber of aspect ratio 8. The values of V_c, G, S_c and λ are kept fixed and R is varied from small to large values. The following values are taken for the fixed parameters,

$$S_c=20,\ G=10^{-2},\ V_c=10\ \text{and}\ \lambda=8 \tag{23}$$

(see Table I). For $R=125$, the plume extends over less than half of the depth of the chamber. The blob which appears at an early stage soon disappears and the final solution becomes steady as shown in Fig. 13(a). When the gyrotaxis number is varied (see Sec. IV B), we have seen that when the plume is short and G is small and $R=500$, it becomes unstable via a meandering instability. However at this small value of R, the

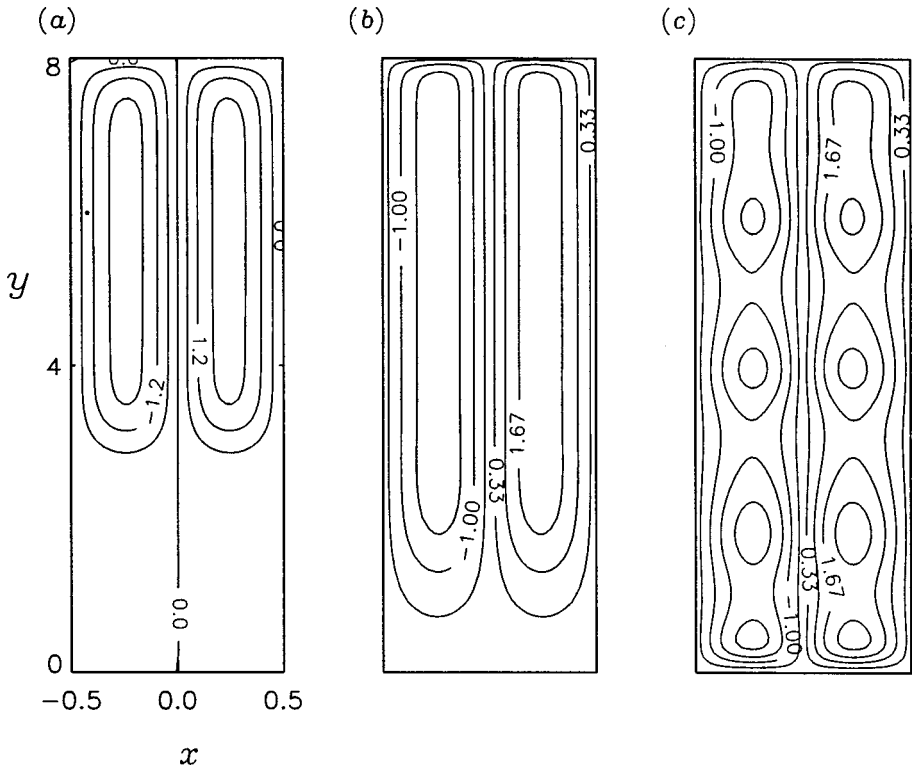

FIG. 12. Dependence of the plume on cell swimming speed in a deep chamber of aspect ratio $\lambda = 8$; snapshots of streamlines for (a) $V_c = 5$, (b) $V_c = 8$, (c) $V_c = 12$. In (a) and (b) the final state is steady but in (c) there is periodic blob convection along the plume. (See also Fig. 8, where $V_c = 10$.)

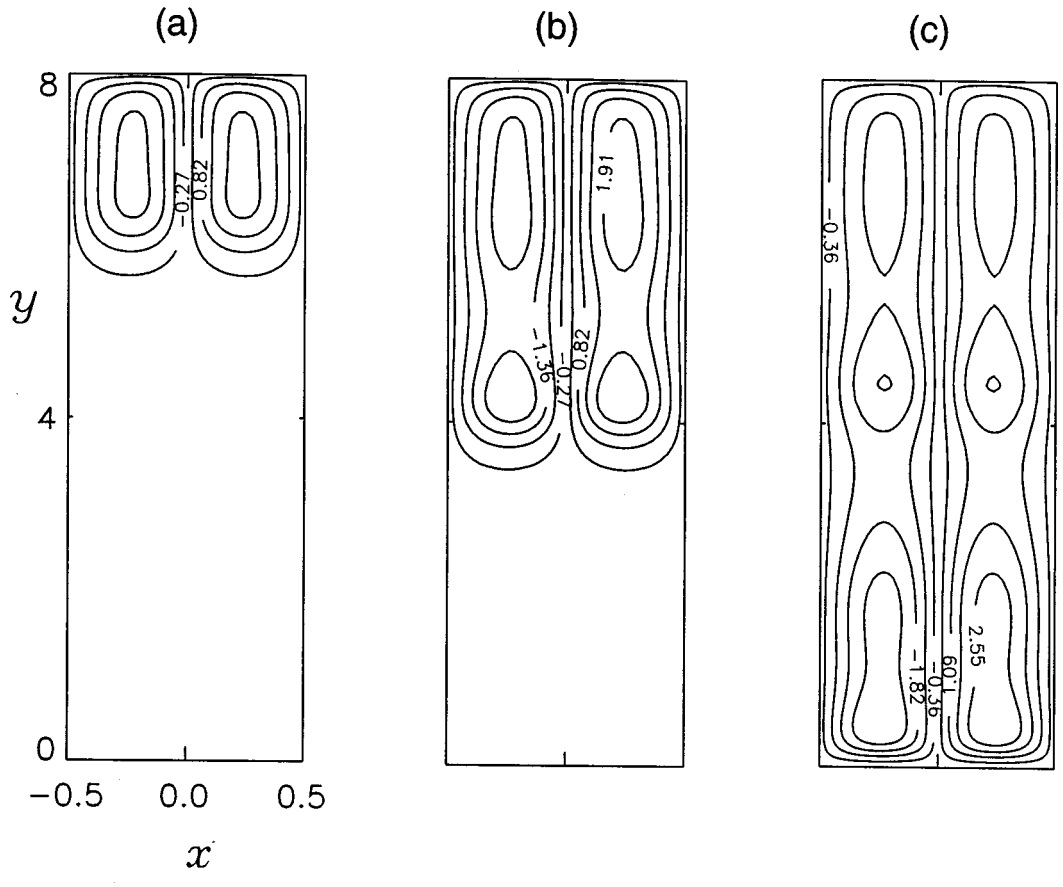

FIG. 13. Dependence of the plume on Rayleigh number in a deep chamber of aspect ratio $\lambda = 8$; snapshots of streamlines for (a) $R = 125$, (b) $R = 250$ and (c) $R = 750$. In (a) the final state is steady but in (b) and (c) there is periodic blob convection along the plume. (See also Fig. 8, where $R = 500$.)

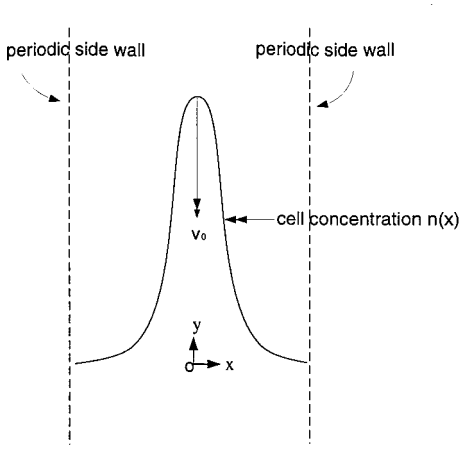

FIG. 14. Geometry of plume located in $-1/2 \leqslant x \leqslant 1/2$. Schematic diagram of concentration profile. v_0 is the central downward speed of the plume.

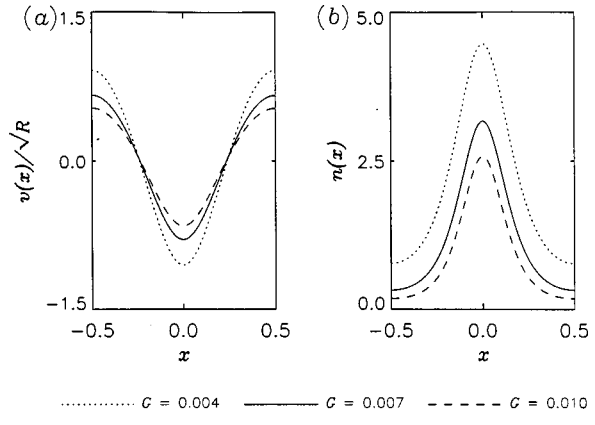

FIG. 15. Basic velocity (a) and concentration (b) profiles for an infinitely long plume for different values of G in a flow between periodic side walls. Here $R=500$, $V_c=10$, $Q_f=0$ and $Q_c=0$.

final state of the plume is steady. Thus the meandering instability is not only related to the length of the plume, but depends on the other parameter values. When $R=250$, the plume extends down to almost half of the chamber depth and a blob convects along the plume periodically [Fig. 13(b)]. Again this differs from the gyrotaxis case. We have seen that the final state of the plume is steady (see Sec. IV B) for a plume extending to almost three-quarter of the depth of the chamber, but here the plume extends only down to half the depth and still the final state is periodic. Thus the blob (varicose) instability also depends on the other parameter values as well as the length of the plume. It was shown in Sec. IV A that at $R=500$, the plume almost extends down to the bottom of the chamber and the final state is periodic with two blobs convecting along the plume. This blob convection persists at $R=750$, but the cell concentration at the bottom of the chamber increases. Figure 13(c) shows a snapshot of this periodic blob convection.

V. LINEAR STABILITY ANALYSIS

We have seen two kinds of instabilities in a large aspect ratio chamber. In order to understand these instabilities better, a model for an infinitely long plume is derived and its linear stability is tested. The linear stability analysis is valid only when the cells do not tumble so that G cannot be too large. The governing equations are Eqs. (10)–(12) with the swimming direction given by

$$\overline{\boldsymbol{p}}=(-G\zeta,(1-G^2\zeta^2)^{1/2}).$$

A. The primary flow

The basic flow configuration is sketched in Fig. 14. Because of symmetry, the primary flow is solved only in the region $0 \leqslant x \leqslant 1/2$. The upwards velocity $v(x)$ is greatest at $x=1/2$ and least at $x=0$. Thus,

$$\zeta(x)=\frac{dv}{dx}=0 \text{ at } x=0, 1/2, \tag{24}$$

whereas the concentration is greatest at $x=0$ and least at $x=1/2$ so that

$$\frac{dn}{dx}=0 \text{ at } x=0, 1/2. \tag{25}$$

Also the total nondimensional fluid flux, Q_f, and the total nondimensional cell flux, Q_c, are prescribed. The values of both Q_f and Q_c are zero for the numerical experiments, which implies that

$$2\int_0^{1/2} v(x)dx=Q_f=0 \tag{26}$$

and

$$2\int_0^{1/2} [v(x)+V_c(1-G^2\zeta^2)^{1/2}]n(x)dx=Q_c=0. \tag{27}$$

From Eqs. (10)–(12) for bioconvection and the boundary conditions given by Eqs. (24) and (25), we obtain

$$\frac{d^3v}{dx^3}=R\frac{dn}{dx} \tag{28}$$

and

$$\frac{dn}{dx}=-V_cG\frac{dv}{dx}n. \tag{29}$$

Equation (28) represents a balance between viscous diffusion and buoyancy and Eq. (29) represents a balance between the horizontal diffusive and the horizontal gyrotactic cell fluxes. Equations (26)–(29) have been solved for a given set of parameter values (Ghorai and Hill[18]). Figure 15 shows the basic flows for different values of G, the gyrotaxis number. The peak cell concentration is relatively low for large G and vice versa.

B. The linear stability problem

We consider a small perturbation of amplitude ϵ ($0<\epsilon \ll 1$) to the primary flow (see Sec. V A with $Q_f=0$ and $Q_c=0$), so that

$$\psi=\psi(x)+\epsilon\psi^*(x,y,t),\ n=n(x)+\epsilon n^*(x,y,t), \tag{30}$$

and look for normal modes of the form

$$\psi^* = \phi(x)\exp(i\alpha(y-ct)) \text{ and}$$

$$n^* = \theta(x)\exp(i\alpha(y-ct)).$$

Substituting into the governing Eqs. (10)–(12) and linearizing about the basic state gives at $O(\epsilon)$

$$D^4\phi = -RD\theta + \left\{2\alpha^2 - \frac{i\alpha c}{S_c} + \frac{i\alpha v(x)}{S_c}\right\}D^2\phi + \left\{\frac{i\alpha^3 c}{S_c} - \frac{i\alpha}{S_c}\frac{d\zeta}{dx} - \frac{i\alpha^3 v(x)}{S_c} - \alpha^4\right\}\phi \tag{31}$$

and

$$D^2\theta = -V_c G\zeta(x)D\theta + \left\{\alpha^2 - i\alpha c + i\alpha v(x) - V_c G\frac{d\zeta}{dx} + i\alpha V_c(1-G^2\zeta^2)^{1/2}\right\}\theta + V_c G n(x)D^3\phi + \left\{V_c G\frac{dn}{dx} + \frac{i\alpha V_c G^2\zeta(x)n(x)}{(1-G^2\zeta^2)^{1/2}}\right\}D^2\phi - \alpha^2 V_c G n(x)D\phi + \left\{i\alpha\frac{dn}{dx} - \alpha^2 V_c G\frac{dn}{dx} - \frac{i\alpha^3 V_c G^2\zeta(x)n(x)}{(1-G^2\zeta^2)^{1/2}}\right\}\phi, \tag{32}$$

where $D \equiv d/dx$. The boundary conditions are

$$D^i\phi(-1/2) = D^i\phi(1/2), \quad i = 0, \ldots, 3, \tag{33}$$

$$D^i\theta(-1/2) = D^i\theta(1/2), \quad i = 0,1, \tag{34}$$

where $D^i \equiv d^i/dx^i$. The boundary conditions are satisfied by both the varicose and the meandering modes. To investigate these modes separately, we specify the following boundary conditions in the half-region $0 \leqslant x \leqslant 1/2$. The boundary conditions corresponding to the varicose mode are

$$\phi = D^2\phi = D\theta = 0 \text{ at } x = 0,\ 1/2 \tag{35}$$

and

$$\theta = 1 \text{ at } x = 0. \tag{36}$$

These boundary conditions are the same as for the varicose mode in the stress-free side walls case (Ghorai and Hill[18]). The boundary conditions corresponding to the meandering mode are

$$D\phi = D^3\phi = \theta = 0 \text{ at } x = 0,\ 1/2 \tag{37}$$

and

$$D^2\phi = 1 \text{ at } x = 0. \tag{38}$$

Equations (31) and (32) together with the boundary conditions specify an eigenvalue problem for c as a function of the dimensionless parameters R, S_c, V_c, G, and α, and the instability grows whenever $\mathrm{Im}(c) > 0$. Solutions to the full linear stability problem are calculated with a fourth-order accurate, finite-difference scheme provided by Dr. D. R. Moore (Cash and Moore[26]). This scheme is used to compute (i) neutral curves for which $\mathrm{Im}(c) = 0$, and (ii) the growth rate as a function of α for given parameters values. Initially, values of R, G, V_c, S_c, and α are supplied and the values of c, ϕ, and θ, are estimated either from the asymptotic results, or from the previous numerical results, or by imposing a sinusoidal variation in $\phi(x)$ and $\theta(x)$. Once a solution is obtained, this solution can be used as an initial guess for the neighboring parameter values. The dependence of the numerical solutions on the number of grid points was tested for different parameter values.

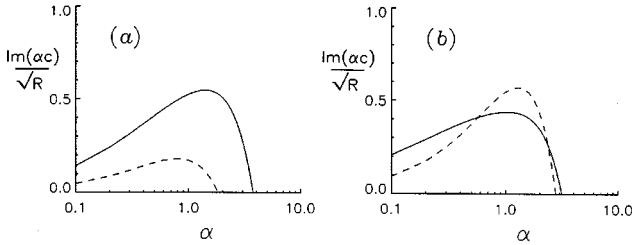

FIG. 16. Growth rates of the varicose (—) and meandering (- - -) modes for (a) $G = 6\times10^{-3}$ and (b) $G = 2\times10^{-3}$. Here $R = 500$, $V_c = 10$, $Q_f = 0$ and $Q_c = 0$.

C. Linear stability results

1. Effect of the gyrotaxis number

The growth rate curves for two different values of G are plotted in Fig. 16. For large values of G [see Fig. 16(a)], the varicose instability dominates the meandering instability. However for small values of G [see Fig. 16(b)], there is a crossover in growth rates between the varicose and the meandering modes. Hence, for small values of G, the competition between the modes depends on the wavelength of the instability, and the meandering mode is the most unstable overall. The plume is unconditionally stable $[\mathrm{Im}(c) < 0]$ at sufficiently large wave numbers (small wavelengths).

Figure 17 shows the stability diagram in the $G\alpha$-plane. The plane can be divided into five regions. In region I, the plume is unstable to both the varicose and the meandering modes, but the growth rate of the meandering mode (Mg) is greater than that of the varicose mode (Vg). On the other hand, the plume is unstable only to the meandering mode in the region III. Thus for small values of G, the plume becomes unstable via a meandering instability. The plume is

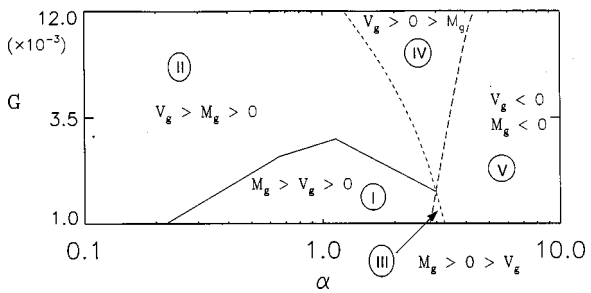

FIG. 17. Stability diagram in the $G\alpha$-plane for periodic side walls. Here $R = 500$, $V_c = 10$, $Q_f = 0$, and $Q_c = 0$. The growth rate of the varicose mode (Vg) is zero on the long-dashed line and that of the meandering mode (Mg) on the short-dashed line, and $Vg = Mg$ on the solid line. Both axes are in logarithmic units.

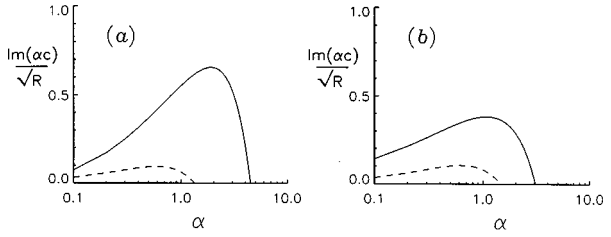

FIG. 18. Growth rates of the varicose (—) and meandering (- - -) modes for (a) $V_c=12$ and (b) $V_c=5$. Here $R=500$, $G=0.01$, $Q_f=0$ and $Q_c=0$.

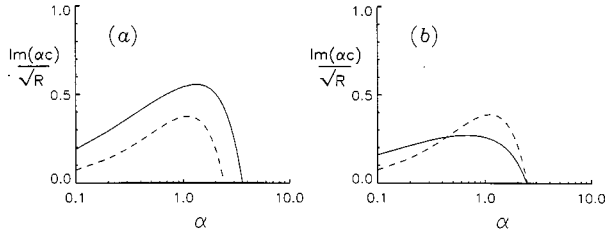

FIG. 20. Growth rates of the varicose (—) and meandering (- - -) modes for (a) $V_c=12$ and (b) $V_c=5$. Here $R=500$, $G=3\times10^{-3}$, $Q_f=0$ and $Q_c=0$.

unstable to the varicose mode for large values of G (regions II and IV) and is unconditionally stable at sufficiently small wavelengths (region V). The varicose instability dominates the meandering instability in most of the unstable region.

2. Effect of the cell swimming speed

The growth rate curves associated with two different values of V_c, the cell swimming speed, when $G=0.01$ are shown in Fig. 18. The varicose mode is the most unstable mode for the values of the parameters considered. The growth rate of the varicose (meandering) mode increases (decreases) with an increase in the value of V_c. The plume is unconditionally stable at sufficiently small wavelengths.

The stability diagram in the $V_c\alpha$-plane (see Fig. 19) is divided only into three regions and the growth rate of the varicose mode is always greater than that of the meandering mode. Thus the plume becomes unstable via a varicose instability in the regions I and II and is unconditionally stable at sufficiently small wavelengths (region III).

The above stability diagram is also a function of other parameter values. The growth rate curves for the values of V_c corresponding to Fig. 18, but with $G=3\times10^{-3}$ instead of $G=0.01$, are plotted in Fig. 20. Here we see that the meandering mode dominates the varicose mode for smaller values of V_c over a range of wavelengths. This figure is similar to Fig. 16 when the gyrotaxis number was varied and so the $V_c\alpha$-plane is divided into five regions for $R=500$, $G=3\times10^{-3}$, $Q_f=0$, and $Q_c=0$. Thus the meandering mode is dominant for small values of G and V_c.

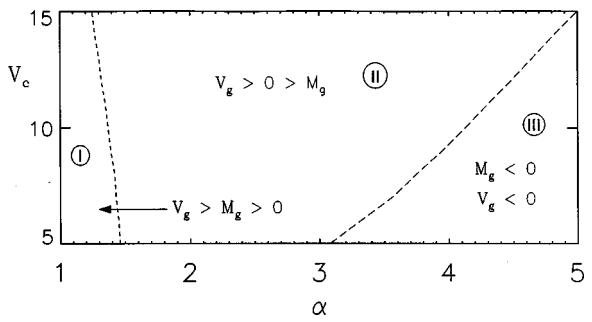

FIG. 19. Stability diagram in the $V_c\alpha$-plane for periodic side walls. Here $R=500$, $G=0.01$, $Q_f=0$ and $Q_c=0$. The growth rate of the varicose mode (Vg) is zero on the long-dashed line and that of the meandering mode (Mg) on the short-dashed line.

D. Instability mechanism

The instability associated with the varicose mode leads to blob formation and that with the meandering mode leads to sinuous movement of the plume. The wavelength of the most unstable mode when $R=500$, $V_c=10$, $G=2\times10^{-3}$, $Q_f=0$, and $Q_c=0$ is approximately 5.7 for the varicose instability and approximately 4.8 for the meandering instability. The contours of the perturbed concentration field at these two wavelengths are plotted in Fig. 21.

The mechanism for the varicose instability is shown schematically in Fig. 22. The bulging region of the plume corresponds to positively perturbed concentration and the narrow region corresponds to negatively perturbed concentration. The region of higher cell concentration sinks downwards because it is more negatively buoyant, and causes circulations as shown at the top of Fig. 22. These circulations attract more cells due to gyrotaxis from nearby and reinforce the bulging region. The region of lower concentration induces circulations in the opposite sense and hence the concentration in that region depletes further. The varicose modes of the solutions with periodic side walls and stress-free side walls are same, since the varicose solution with stress-free side walls (see Ghorai and Hill[18]) is symmetric about the mid-vertical plane. Ghorai and Hill[18] have shown that gyrotaxis is necessary for this instability to occur.

The mechanism for the meandering instability is shown schematically in Fig. 23. The region where the plume bends outwards sinks because it is more negatively buoyant and causes circulation as shown in the figure. These circulations cause accumulation of cells in the regions shown by downward pointing arrows and depletion of cells in the opposite sides. Thus we see that gyrotaxis enhances ''snakelike'' wave formation. The two small circulations on both sides of the big circulation are due to the periodic boundary conditions, because the perturbed velocities must be same at the side walls. In the case of stress-free side walls, the perturbed vertical velocity fields at the side walls can be different from each other and the small circulations are not found. These small circulations resist the plume's meandering movement and are the cause of much lower growth rate of the meandering mode than that of the stress-free side walls (Ghorai and Hill[18]).

VI. CONCLUSIONS

The final state of a periodic array of two-dimensional gyrotactic plumes can be either steady or unsteady depend-

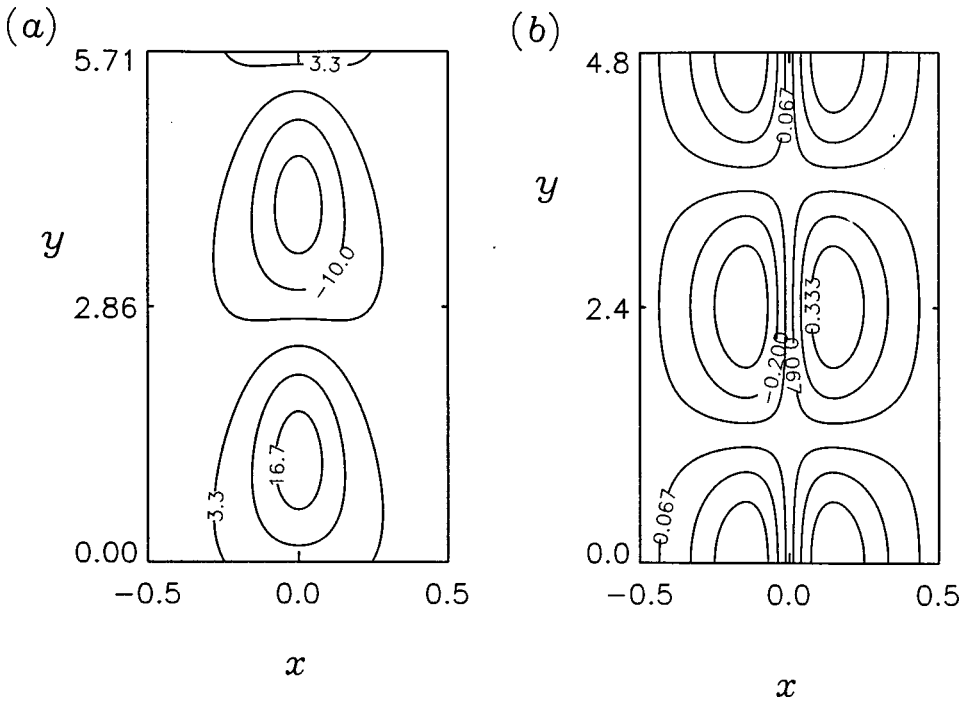

FIG. 21. Contours of the perturbed concentration $n'(x,y)$ for the (a) varicose and (b) meandering instabilities. Here $R=500$, $G=2\times10^{-3}$, $V_c=10$, $Q_f=0$, and $Q_c=0$. Note the different vertical scales.

ing on the parameter values for the suspension of swimming micro-organisms. When it is unsteady, two modes are seen. There is a periodic varicose mode in which blobs convect down each plume and a meandering mode which is quasi-periodic. The final state for a single plume in a chamber with stress-free side walls can also be steady or exhibit varicose and meandering modes (Ghorai and Hill[18]). However, the meandering mode always dominates the varicose mode for deep chambers with stress-free side walls for any set of parameter values whereas the varicose mode is dominant for periodic side walls for certain ranges of parameter values.

The linear stability analysis for an infinitely long plume gives a useful guide for interpreting the stability of a finite plume to gyrotactic instabilities, i.e. instabilities whose dynamics depend on the local stability of the mid-section of the plume away from the top and bottom of the finite depth chamber. This is because the basic plume solution in the mid-section of the chamber is essentially independent of the vertical coordinate, and the horizontal flux of the cells into the plume balances the horizontal component of the diffusion flux out of the plume, just as in the basic state for the infinite plume. As shown below, when an instability of the finite plume occurs, its wavelength is constrained by the top and bottom boundaries but it is otherwise consistent with prediction from the theory for the infinite plume.

In the linear stability analysis, varicose and meandering perturbations are applied to the basic infinitely long plume but, for the finite-depth plume, the perturbations arise naturally during the computation. Initially, the cells are uniformly dispersed throughout the chamber and swim upwards to form concentrated layer of cells at the top of the chamber. This becomes unstable and a plume starts to form and to descend. This initial plume is not independent of z but is usually symmetric about $x=0$. The z-variation can trigger the varicose or blob instability. The meandering mode is usually triggered by rounding errors in the calculations which break the symmetry of the numerical solution.

Notwithstanding the differences between the linear stability analysis and the finite depth computations, the linear stability analysis can predict the possible state of the numerical solution in a sufficiently deep chamber. For example, if

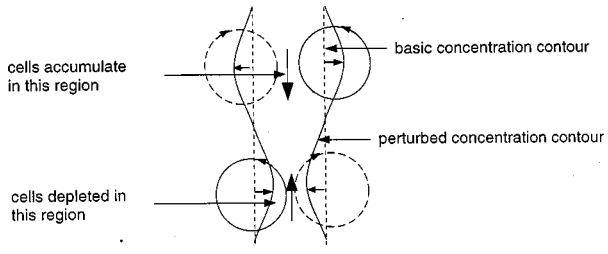

FIG. 22. Mechanism for varicose instability. The regions marked with downward (upward) pointing arrows are more (less) negatively buoyant and causes circulation in the sense shown in the figure.

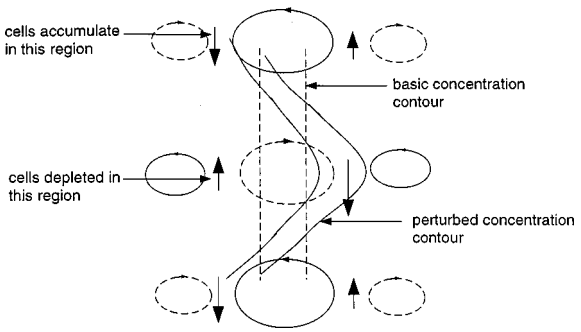

FIG. 23. Mechanism of meandering instability for periodic side walls. The regions marked by downward (upward) pointing arrows are more (less) negatively buoyant.

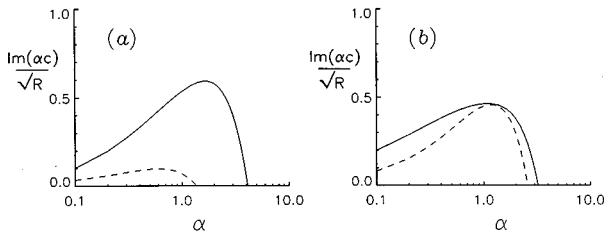

FIG. 24. Growth rates of the varicose (—) and meandering (- - -) modes as functions of the wave number α for (a) $G=0.01$ and (b) $G=2.5\times10^{-3}$. Here $R=500$, $V_c=10$, $Q_f=0$ and $Q_c=0$.

the growth rate of the varicose mode is higher than that of the meandering mode, the final state of numerical solution can be either periodic blob convection or steady-state but not meandering. On the other hand, if the growth rate of the meandering mode is higher than or comparable to that of the varicose mode, the final state is a quasiperiodic meandering plume.

We have plotted the linear stability growth rate curves in Fig. 24(a) for the parameter values shown in the caption of the figure, which were used in the numerical experiments in Sec. IV A to examine the effect of the aspect ratio on the plume's structure and stability. For the varicose mode, the critical wavelength is approximately 1.5 and the most unstable wavelength is approximately 4 or, in dimensional terms, a wavelength of 2 cm when the chamber width is 0.5 cm. For the meandering mode, the critical wavelength is approximately 4.5 and the most unstable wavelength is approximately 10.5. In the numerical experiments in a chamber with finite depth, a varicose mode for $\lambda=2$ occurs during the evolution of the plume, but this ultimately disappears. This is presumably due to the constraints imposed by the boundary conditions at the top and bottom of the chamber. The number of blobs convecting along the plume is one for aspect ratio 5. When the aspect ratio is increased to 8, the number of blobs convecting along the plume is 2. The wavelength of the varicose mode is the distance between two blobs which is a little less than 4 for aspect ratios 5 and 8. This wavelength is consistent with the most unstable wavelength predicted by the linear stability analysis. No meandering mode is seen in the numerical experiments since the growth rate of the varicose mode is greater over the whole range of wavelengths [Fig. 24(a)].

When $G=2.5\times10^{-3}$, the linear stability theory [Fig. 24(b)] shows that the growth rates of the most unstable wavelengths for the varicose and the meandering modes are equal and approximately 6. In contrast, when $G=6\times10^{-3}$, Fig. 16(a) shows that the varicose mode is the most unstable and the wavelength of the most unstable mode is again approximately 6. In the numerical experiments when $\lambda=8$ and $G=2.5\times10^{-3}$ or 6×10^{-3} (see Sec. IV B), the varicose mode appeared early on during the evolution of the plume. When $G=6\times10^{-3}$, the final state was steady although the linear stability theory suggests that a varicose mode should be seen, and when $G=2.5\times10^{-3}$ the final state meanders quasiperiodically without any blobs but the linear stability suggests that a mixed mode might be present. The reasons that the plume for $G=2.5\times10^{-3}$ develops into a meandering mode are probably the following. First, the linear stability growth rate of the meandering mode is comparable to that of the varicose mode. Second, since the plume only extends down to half of the chamber depth, the concentration at the top of the plume is relatively high. This high concentration at the top amplifies the growth rate of the meandering mode. To support the argument that the blobs in the numerical experiments disappear due to the finite depth rather than some other nonlinear behavior, we performed the following numerical experiments in chambers which are periodic in *both* the x and y-directions.

We consider two numerical experiments corresponding to $G=6\times10^{-3}$ and $G=2.5\times10^{-3}$ with their basic flows as the initial conditions. We superimpose small sinusoidal perturbations in both the x and y-directions for both values of G. The streamlines for $G=6\times10^{-3}$ at three different times are shown in Fig. 25. We see that the instability sets in at $t\approx1.0$, which is evident from the departure of the streamlines from the basic vertical state. The next two figures show that the instability grows as a varicose mode and a blob begins to convect along the plume periodically. The varicose instability, due to its much larger growth rate, suppresses the meandering instability. Figure 26 shows the streamlines corresponding to $G=2.5\times10^{-3}$ at three different times. We see that the instability sets in at $t\approx1.2$, which is longer than the time for $G=6\times10^{-3}$, since the growth rates are smaller. Figures 26(b) and 26(c) show that this instability grows as a combined varicose and meandering mode, since their growth rates are almost equal at a wavelength of 6. Thus the linear stability theory is able to predict which modes are seen in these numerical experiments, suggesting that nonlinear effects are not important in the selection of the instability modes.

The role of the gyrotaxis number can be interpreted as follows. Increasing $G=BD/L^2$, keeping the width L and other parameters fixed, implies an increase in the value of B (the gyrotactic reorientation parameter) alone since D involves other parameters in the problem. Now $B=4\pi\mu a^3/mgh\approx3.4$ s assuming $h\approx2\%$ of the cell radius. If the cell is the most bottom-heavy possible, i.e., the center of mass is at the circumsphere, the value of B would be approximately 0.14 s. On the other hand, if the cell becomes less bottom-heavy, the value of B increases and ultimately becomes very large. For small values of G (more bottom-heavy cells), the cells swim upwards preferably and are less prone to focus laterally into the plume. If G is large (less bottom-heavy cells), the viscous torque exceeds gravitational torque and as a result the cells tend to tumble. Tumbling cells are also less prone to focus laterally into the plume. As G is increased from small to intermediate values, the blob instability increases as the cells attracted to the plume more. If G is much higher the blob instability should decrease which has been seen in the numerical experiments (Sec. IV B). The linear stability theory is not valid for the tumbling cells and cannot predict this effect.

We have examined (Sec. IV C) the effect of the cell swimming speed V_c on the plume's stability keeping the values of R, G, S_c, and λ constant. The linear stability

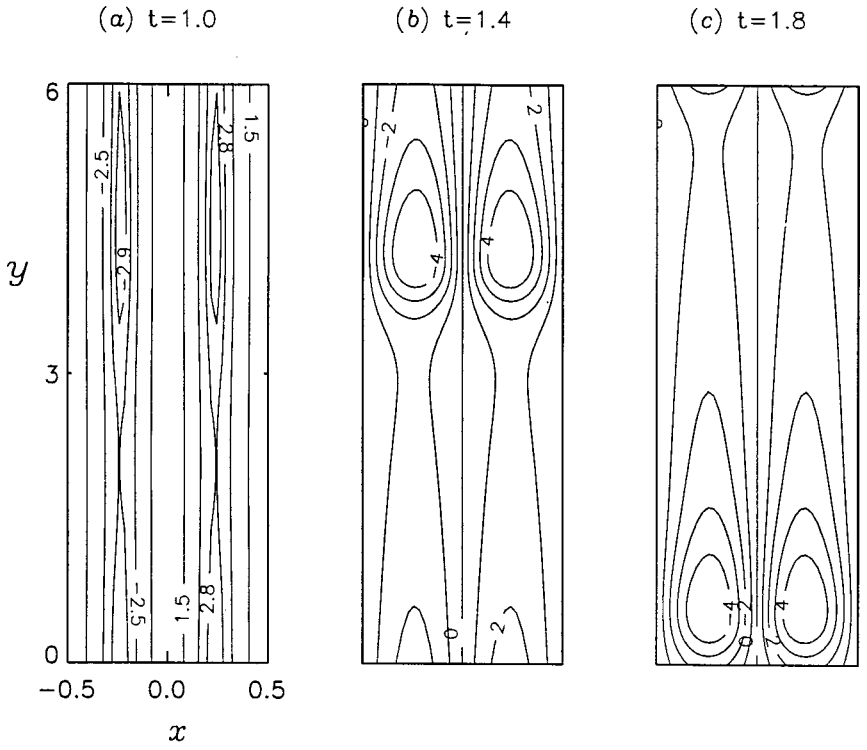

FIG. 25. Streamlines patterns at $t=1.0$, $t=1.4$, and $t=1.8$ in a periodic box of aspect ratio 6 for $G=6\times10^{-3}$, $R=500$ and $V_c=10$.

growth rate curves for $V_c=5$, 10, and 12, with the same set of the other parameter values, are plotted in Figs. 18(b), 24(a), and 18(a), respectively. The numerical solution is steady for $V_c=5$ and consists of periodic blob convection for $V_c=10$ and 12. There is no meandering mode in the numerical experiments since the growth rate of the varicose mode is greater compared to the meandering mode as predicted by the linear stability theory. The varicose mode disappeared at $V_c=5$ due to the constraints imposed by the finite depth of the chamber.

The physical significance of increasing V_c has the following meaning. Increasing $V_c=W_cL/D$, keeping the length scale and the other parameters fixed, results in increasing the cells' swimming speed alone, since D occurs in the other

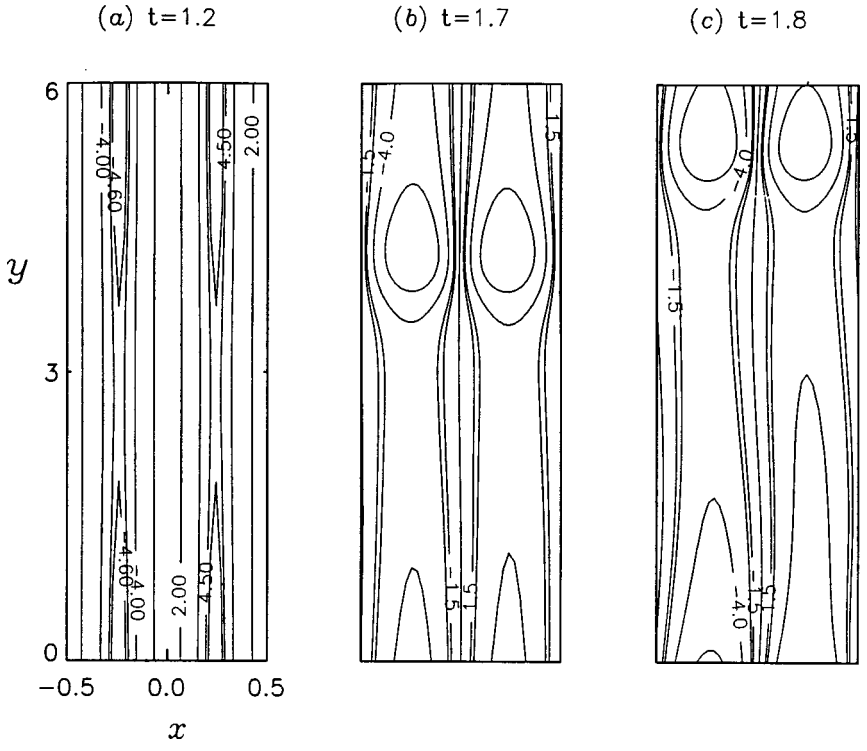

FIG. 26. Streamlines patterns at different times in a periodic box of aspect ratio 6 for $G=2.5\times10^{-3}$, $R=500$ and $V_c=10$.

parameters of the problem. For higher cell swimming speeds, the concentration at the top of the layer increases due to the top boundary. Consequently more cells are swept down the plume by advection at higher values of V_c. The focusing of the cells into the plume increases too since the horizontal swimming is proportional to the swimming speed. Thus as V_c is varied from small to large values, the blob instability becomes more dominant. This has been observed both in the numerical experiments and in the linear stability analysis.

In numerical experiments, we have also examined (Sec. IV D) the effect of varying the Rayleigh number, R, in a fixed aspect ratio chamber. The increase in the value of R can be considered as an increase in the concentration. For $R=125$, the plume extended to almost a quarter of the depth of the chamber and was steady. The solution consisted of a single blob convecting along the plume and extended to almost half the depth of the chamber for $R=250$. For $R=500$, the solution consisted of two-blob convection and the plume extended down to the bottom of the chamber. We have seen that the solution in the mid-region of the steady plume is independent of the vertical coordinate and the balance is between the horizontal component of the diffusive and gyrotactic fluxes. The effect of increasing R in the numerical experiments is to extend the plume's length until it reaches the bottom of the chamber and to change the concentration at the top and bottom whilst keeping the concentration fixed in the mid-region of the chamber. The length of the plume (i.e. the distance between the top and bottom of the plume) when $R=125$ was less than the critical wavelength of the varicose mode which led to the steady-state solution. As the length of the plume increased with an increase in the value of R, we saw one blob followed by two blobs due to the selection of the most unstable wavelength of the varicose mode.

Fully three-dimensional calculations have yet to be carried out. Studies of axisymmetric bioconvection in a cylindrical chamber (Ghorai[20]) show only the varicose instability due to the imposed symmetry but the physics of the instability and the dependence of the solution on the parameters has much in common with the two-dimensional case. Meandering and varicose modes are seen in experiments (Pedley and Kessler[1]) and this work does appear to explain successfully the mechanisms and the competitions between the modes of instability. Detailed quantitative comparisons must await further experimental data but the predicted wavelengths and time scales are consistent with casual estimates from experiments.

ACKNOWLEDGMENTS

S. G. gratefully acknowledges funding from an Overseas Research Studentship and from the Tetley and Lupton Foundation of the University of Leeds.

[1] T. J. Pedley and J. O. Kessler, ''Hydrodynamic phenomena in suspensions of swimming micro-organisms,'' Annu. Rev. Fluid Mech. **24**, 313 (1992).
[2] J. O. Kessler, ''Hydrodynamic focusing of motile algal cells,'' Nature (London) **313**, 218 (1985).
[3] J. R. Platt, ''Bioconvection patterns in cultures of free-swimming organisms,'' Science **133**, 1766 (1961).
[4] M. S. Plesset and H. Winet, ''Bioconvection patterns in swimming microorganism cultures as an example of Rayleigh–Taylor instability,'' Nature (London) **248**, 441 (1974).
[5] J. O. Kessler, ''Cooperative and concentrative phenomena of swimming micro-organisms,'' Contemp. Phys. **26**, 147 (1985).
[6] S. Childress, M. Levandowsky, and E. A. Spiegel, ''Pattern formation in a suspension of swimming micro-organisms: Equations and stability theory modes,'' J. Fluid Mech. **69**, 595 (1975).
[7] T. J. Pedley, N. A. Hill, and J. O. Kessler, ''The growth of bioconvection patterns in a uniform suspension of gyrotactic micro-organisms,'' J. Fluid Mech. **195**, 223 (1988).
[8] H. Wager, ''On the effect of gravity upon the movements and aggregation of *Euglena viridis*, Ehrb., and other micro-organisms,'' Philos. Trans. R. Soc. London, Ser. B **201**, 333 (1911).
[9] J. B. Loeffer and R. B. Mefferd, ''Concerning pattern formation by free-swimming micro-organisms,'' Am. Nat. **86**, 325 (1952).
[10] J. J. Wille and C. F. Ehret, ''Circadian rhythm of pattern formation in population of a free-swimming organism, *Tetrahymena*,'' J. Protozool. **15**, 789 (1968).
[11] J. O. Kessler, ''Gyrotactic buoyant convection and spontaneous pattern formation in algal cell cultures,'' in *Non-Equilibrium Cooperative Phenomena in Physics and Related Fields*, edited by M. G. Velarde (Plenum, New York, 1984), p. 241.
[12] M. A. Bees and N. A. Hill, ''Wavelengths of bioconvection patterns,'' J. Exp. Biol. **200**, 1515 (1997).
[13] N. A. Hill and D.-P. Häder, ''A biased random walk model for the trajectories of swimming micro-organisms,'' J. Theor. Biol. **186**, 503 (1997).
[14] T. J. Pedley and J. O. Kessler, ''A new continuum model for suspensions of gyrotactic micro-organisms,'' J. Fluid Mech. **212**, 155 (1990).
[15] G. K. Batchelor, ''The stress system in a suspension of force-free particles,'' J. Fluid Mech. **41**, 545 (1970).
[16] T. J. Pedley and J. O. Kessler, ''The orientation of spheroidal microorganisms swimming in a flow field,'' Proc. R. Soc. London, Ser. B **231**, 47 (1987).
[17] A. Harashima, M. Watanabe, and I. Fujishiro, ''Evolution of bioconvection patterns in a culture of motile flagellates,'' Phys. Fluids **31**, 764 (1988).
[18] S. Ghorai and N. A. Hill, ''Development and stability of gyrotactic plumes in bioconvection,'' J. Fluid Mech. **400**, 1 (1999).
[19] M. A. Bees, N. A. Hill, and T. J. Pedley, ''Analytical approximations for the orientation distribution of small dipolar particles in steady shear flows,'' J. Math. Biol. **36**, 269 (1998).
[20] S. Ghorai, ''Bioconvection and plumes,'' Ph.D. thesis, University of Leeds, 1997.
[21] J. O. Kessler, ''Individual and collective fluid dynamics of swimming cells,'' J. Fluid Mech. **173**, 191 (1986).
[22] N. A. Hill, T. J. Pedley, and J. O. Kessler, ''Growth of bioconvection patterns in a suspension of gyrotactic mirco-organisms in a layer of finite depth,'' J. Fluid Mech. **208**, 509 (1989).
[23] Kálnay de Rivas, ''On the use of nonuniform grids in finite-difference equations,'' J. Comput. Phys. **10**, 202 (1972).
[24] G. O. Roberts, ''Computational meshes for boundary layer problems,'' in *Second International Conference on Numerical Methods in Fluid Dynamics*, Lecture Notes in Physics, edited by M. Holt (Springer, New York, 1970), Vol. 8, p. 171.
[25] G. de Vahl Davis, ''Natural-convection of air in a square cavity: A benchmark numerical-solution,'' Int. J. Numer. Methods Fluids **3**, 249 (1983).
[26] J. R. Cash and D. R. Moore, ''A high order method for the numerical solution of two point boundary value problems,'' BIT **20**, 44 (1980).